Catalysis Today 148 (2009) 260–267

Contents lists available at ScienceDirect

Catalysis Today

journal homepage: www.elsevier.com/locate/cattod

DFT studies of dry reforming of methane on Ni catalyst

Yi-An Zhu [a], De Chen [b,*], Xing-Gui Zhou [a,*], Wei-Kang Yuan [a]

[a] UNILAB, State Key Laboratory of Chemical Engineering, East China University of Science and Technology (ECUST), 130 Meilong Rd., Shanghai 200237, China
[b] Department of Chemical Engineering, Norwegian University of Science and Technology (NTNU), N-7491 Trondheim, Norway

ARTICLE INFO

Article history:
Available online 23 October 2009

Keywords:
Density functional theory
Dry reforming
Nickel
Carbon dioxide

ABSTRACT

First-principles calculations based on density functional theory (DFT) have been used to investigate the reaction mechanism of dry methane reforming on Ni(1 1 1). The most energetically favorable adsorption configurations of the species involved in this process are identified and the transition states for all the possible elementary steps are explored by the dimer method. Then, the related thermodynamic properties at 973.15 K are calculated by including the zero-point energy correction, thermal energy correction and entropic effect. It is found that CO_2 dissociates via a direct pathway to produce CO and O dominantly, and atomic O is revealed to be the primary oxidant of CH_x intermediates. Based on this information, two dominant reaction pathways are constructed as both the CH and C oxidation are found to be likely. The reaction network begins with the dissociation of CO_2 and CH_4, and then the generated CH and C are oxidized by atomic O to produce CHO and CO, followed by the CHO decomposition to finally generate CO and H_2. As for these two reaction pathways, the oxidation step is predicted to determine the overall reaction rate under the current investigated conditions, while the CH_4 dissociation is found to be the rate-limiting step at lower temperatures.

1. Introduction

Dry reforming of methane has received much attention of the scientific community because it produces syngas with low H_2/CO ratio, which can be preferentially used for the synthesis of liquid hydrocarbons in the Fischer–Tropsch synthesis network and for the preparation of high-purity CO [1]. Furthermore, from an environmental perspective, a significant advantage of this process is the utilization of greenhouse gases, CH_4 and CO_2, which are leading to global warming. Finally, many potential thermodynamic heat-pipe applications such as recovery, storage and transmission of solar and other renewable energy sources have been proposed on the basis of the high enthalpy change and reversibility of dry methane reforming [2].

The cheap supported Ni catalyst is regarded as the most attractive catalyst for this process, though some noble metals such as Rh and Ru are found to be more reactive [3–7]. Nevertheless, under the same reaction conditions, the supported Ni catalyst is active for coke formation and growth of filamentous carbon as well [8–10]. Consequently, the severe catalyst deactivation becomes the main obstacle with respect to the commercialization of dry reforming of methane.

Despite numerous experimental and theoretical work devoted to investigating the reaction mechanism of dry methane reforming [6,8,11–24], some questions remain open. For example, it is well known that the role of the co-reactant CO_2 is to provide the oxidants of CH_x (x = 0–3) species, i.e., OH and O. Then, which is the primary oxidant in this reaction? Bradford and Vannice [12] proposed a kinetic model for CH_4-CO_2 reforming which correlates experimental data successfully. In their model, CO_2 participates in the reaction through the reverse water–gas shift (RWGS) reaction to produce OH, and OH group reacts with adsorbed CH_x intermediates to yield formate-type species (CH_xO). In contrast, based on the kinetic and isotopic measurements, Wei and Iglesia [6] argued that C atoms are oxidized by atomic O to form CH_xO which is taken as the most abundant intermediate on the surface.

Secondly, there is a big reaction network available for dry reforming of methane, so the confirmation of the predominant reaction pathway and rate-limiting step is challenging. Rostrup-Nielsen and Hansen [11] declared that steam reforming and dry reforming of methane on Ni catalyst proceed with the same rate, and the CH_4 dissociation and C oxidation are predicted to determine the overall reaction rate. Bradford and Vannice [12] suggested that dry reforming of methane occurs via the reversible dissociation of CH_4 and CO_2 to produce CH_xO, and the decomposition of CH_4 as well as CH_xO is the kinetically slow step. Wei and Iglesia [6] carried out some comparative experiments for the CH_4 dissociation, steam and dry reforming of methane, as well as WGS reaction. They proposed that regardless of the co-reactants, the C–H bond activation is the sole

* Corresponding authors.
E-mail addresses: chen@chemeng.ntnu.no (D. Chen), xgzhou@ecust.edu.cn (X.-G. Zhou).

0920-5861/$ – see front matter © 2009 Elsevier B.V. All rights reserved.
doi:10.1016/j.cattod.2009.08.022

kinetically relevant step in all three reactions, and the steps involving co-reactants turns out to be quasi-equilibrated.

During the past two decades, theoretical work based on density functional theory (DFT) has also been extensively conducted to answer the aforementioned open questions [17–24]. Watwe et al. [17] performed periodic infinite plane wave slab calculations to investigate the stability and reactivity of CH_x species on Ni(1 1 1). Based on the combined DFT calculations and kinetic analyses, it was found all the CH_x species prefer threefold sites and CH as well as CO is the most abundant species on the surface. Michaelides and Hu [18–20] used DFT calculations to study the CH_3 and CH_2 adsorption on Ni(1 1 1), and declared that the C–H–Ni three-center bonding determines the chemisorption sites of CH_3 and CH_2. They also reported that the CH_3 dehydrogenation is exothermic with the reaction heat of −48 kJ/mol and the corresponding activation energy is more than 100 kJ/mol. Bengaard et al. [21] carried out first-principles calculations to suggest that both the CH_4 dissociation and nucleation of graphite are structure-sensitive, and their estimation of the barrier for the CH_4 dissociation is less than 91 kJ/mol. More recently, Blaylock et al. [22] have combined thermodynamic data with electronic activation energies to develop a microkinetic model to simulate steam reforming of methane under realistic conditions. The rate-limiting steps were found to be the CH_4 dissociative adsorption and the CH oxidation by O as well as OH. As for the CO_2 adsorption and decomposition, Wang et al. [23,24] reported that the CO_2 adsorption on Ni(1 1 1) is endothermic and the chemisorbed CO_2 molecule is negatively charged. Furthermore, the same authors suggested a mechanism for dry reforming of methane on the basis of the energy barriers obtained by DFT calculations. Their mechanism included the CO_2 decomposition to generate oxidant (atomic O), the CH_4 dissociation to surface CH, the CH oxidation by O and the CHO decomposition to produce CO, in which the CH_4 dissociation was found to be the rate-limiting step. However, in their calculations, atomic O was taken as the sole oxidant of CH and the contribution of OH was neglected.

In this contribution, the adsorption energies of the related species are firstly calculated by DFT calculations and the transition states for the involved elementary reactions are located by the dimer method [25]. Because Ni catalyst is traditionally used in dry reforming of methane at temperatures of above 973.15 K [26], the corresponding Gibbs free energy barriers at this temperature are then calculated. In order to provide a comprehensive mechanistic picture, the dissociation of CO_2 and CH_4, the oxidation of CH and C, and the decomposition of CHO(H) as well as COH are investigated in detail. Consequently, the predominant reaction pathway and rate-limiting step are revealed. Finally, we conclude by discussing the implication of our results for understanding the overall mechanism of dry reforming of methane on Ni catalyst.

2. Computational details

2.1. DFT calculations

The first-principles calculations performed in this study are based on spin-polarized DFT. The Vienna *ab initio* simulation package (VASP) [27–30] is used, in which the interactions between valence electrons and ion cores are described by pseudopotentials and the electronic wavefunctions at each *k*-point are expanded in terms of a discrete plane-wave basis set. Here we use Blöchl's all-electron-like projector augmented wave (PAW) method [31] as implemented by Kresse and Joubert [32], which regards the 4s 3d states as the valence configuration for Ni, 4d 5s states for Ag, 2s 2p states for C. The PAW method is necessary for accurate calculations of certain transition metals, which are sometimes poorly described by the ultrasoft pseudopotentials. Exchange and correlation of the Kohn–Sham theory are treated with the generalized gradient approximation (GGA) in the formulation of PBE functional [33]. A plane wave energy cutoff of 400 eV is used in the present calculation and all geometries are optimized using a force-based conjugate gradient algorithm [34] until the forces acting on each atom are converged better than 0.01 eV/Å. Brillouin zone sampling is performed using a Monkhorst–Pack grid [35] and electronic occupancies are determined according to a Methfessel–Paxton scheme [36] with an energy smearing of 0.2 eV. Because there is a magnetic element (Ni) involved in the system, spin polarized effect has been considered. The calculations performed by Kresse and Hafner showed that surface magnetism is essential for the accurate quantitative description of adsorption energy [37].

The Ni(1 1 1) surface is represented as a four-layer slab with $p(3 \times 3)$ supercell and only the bottom layer of the slab is constrained to their crystal lattice positions. The neighboring slabs are separated in the direction perpendicular to the surface by a vacuum region of 12 Å. The first Brillouin zone of the $p(3 \times 3)$ supercell is sampled with a $3 \times 3 \times 1$ *k*-point grid, which are evidenced to be sufficient for this cell [38,39].

The Hessian matrix for the potential energy surface is calculated using finite difference approximation, and diagonalized to find the normal modes of the investigated systems. The adsorbates and the metal atoms to which the adsorbates are attached are displaced in the direction of each Cartesian coordinate, while the other Ni atoms are kept rigid during these finite difference calculations because in the preliminary calculation, the CH_4 vibrational frequencies adopt almost the same wavenumbers with and without the relaxation of the metal atoms in the deeper layers.

The dimer method [25] is used to locate the transition state, in which the saddle point is optimized using a force-based conjugate-gradient method [34] until the maximum force in every degree of freedom is less than 0.01 eV/Å. In order to obtain accurate forces, the total energy and band structure energy are converged to within 1×10^{-7} eV/atom during the electronic optimization.

2.2. Thermodynamics

2.2.1. Gas-phase species

The Gibbs free energy of a gas-phase species A [CO_2(g), CH_4(g), H_2(g), CO(g), H_2O(g), CH_3OH(g)] at temperature T and pressure P is given by

$$G_A(T,P) = E_{total,A} + E_{ZPE} + \Delta H^\circ(0 \to T) - TS(T,P)$$
$$= E_{total,A} + E_{ZPE} + \Delta H^\circ(0 \to T) - TS^\circ(T) + RT\ln\left(\frac{P}{P^\circ}\right) \quad (1)$$

where $E_{total,\,A}$ is the total energy determined by DFT calculations. E_{ZPE} is the zero-point energy, which is calculated by

$$E_{ZPE} = \sum_{i=1}^{3N-6(5)} \frac{N_A h\nu_i}{2} \quad (2)$$

where N_A is Avogadro's number, h is Plank's constant, ν_i is the frequency of the normal mode, and N is the number of atoms involved in the system. $\Delta H^\circ(0 \to T)$ is the enthalpy change from 0 K to temperature T. As for CO_2(g), H_2(g), CO(g) and H_2O(g), the enthalpy change from 0 K to 298.15 K can be found in Ref. [40]. The corresponding values of CH_4(g) and CH_3OH(g) are calculated by

$$\Delta H^\circ(0 \to T) = H_{trans} + H_{rot} + (H - E_{ZPE})$$
$$= \frac{5}{2}RT + \frac{3}{2}RT + \sum_{i=1}^{3N-6} \frac{N_A h\nu_i e^{-h\nu_i/k_BT}}{1 - e^{-h\nu_i/k_BT}} \quad (3)$$

where R is the universal gas constant, k_B is Boltzmann's constant. The enthalpy change of a gas-phase species A from 298.15 K to

temperature T and the standard entropy at temperature T [$S^\circ(T)$] are calculated using the Shomate equation and the related parameters are taken from Ref. [40]. P° is the standard pressure which is taken to be 1 bar.

2.2.2. Weakly bound species

The Gibbs free energy for a species A adsorbed on Ni surface is calculated using a similar expression:

$$G_A(T,P) = E_{total,A} + E_{ZPE} + \Delta U^\circ(0 \to T) - TS^\circ(T) \quad (4)$$

where the enthalpy change is replaced by the change of internal energy.

As for the weakly bound species, namely CH_4* and CO_2*, we assume to a first approximation that they behave as two-dimensional gases and maintain the full rotational and vibrational modes of the corresponding gaseous species. The standard internal energy change of adsorption is calculated by

$$\Delta U^\circ_{trans,2D}(0 \to T) - \Delta U^\circ_{trans,3D}(0 \to T) = 2RT - \frac{5}{2}RT = -\frac{1}{2}RT \quad (5)$$

The standard entropy change (ΔS°) of adsorption is calculated by

$$\Delta S^\circ = S^\circ_{trans,2D} - S^\circ_{trans,3D} = R\left[\ln\left(\frac{h/k_BT}{(2\pi m k_B T)^{1/2}}\left(\frac{SA}{N_{sat}}\right)P^\circ\right) - \frac{1}{2}\right] \quad (6)$$

where SA/N_{sat} is the area occupied per adsorbed molecule at the standard state conditions. If it is assumed that the standard state is monolayer coverage, SA/N_{sat} equals the reciprocal of the surface concentration of sites.

2.2.3. Tightly bound species

As for the tightly bound species including the remaining reactants, transition states, intermediates and products, the translational and rotational modes are replaced by vibrational modes corresponding to frustrated translation and rotation on the surface. Consequently, the internal energy change and entropy of the tightly adsorbed species are given by

$$\Delta U^\circ(0 \to T) = \sum_{i=1}^{3N} \frac{N_A h\nu_i e^{-h\nu_i/k_BT}}{1 - e^{-h\nu_i/k_BT}} \quad (7)$$

$$S^\circ(T) = S^\circ(T) = \sum_{i=1}^{3N}\left[-R\ln(1 - e^{-h\nu_i/k_BT}) + \frac{N_A h\nu_i}{T}\frac{e^{-h\nu_i/k_BT}}{(1 - e^{-h\nu_i/k_BT})}\right] \quad (8)$$

3. Results and discussion

Based on the previous work from other research groups [6,11,26], we propose here a more detailed mechanism for dry reforming of methane. The investigated reaction network is schematically illustrated in Fig. 1.

3.1. CO_2 decomposition

As elucidated in the experimental work [6,12], two possible reaction pathways are predicted to contribute to the CO_2 decomposition. As for the first one, the adsorbed CO_2 dissociates directly to form CO and atomic O, the latter being the oxidant of CH_x. Along the second reaction pathway, CH_4 firstly dissociates to produce atomic H which subsequently activates the adsorbed CO_2 by producing the COOH intermediate, and the decomposition of COOH finally yields CO and the oxidant OH, according to

$$CO_2* + H* \to COOH* \to CO* + OH* \quad (9)$$

The calculated adsorption energies (ΔE_{ads}) of the species involved in dry reforming of methane are summarized in Table 1. ΔE_{ads} is calculated as

$$\Delta E_{ads} = E_{adsorbate+surface} - E_{surface} - E_{adsorbate} \quad (10)$$

The first term on the right-hand side is the total energy of the surface with one attached molecule; the second term is the total energy of surface. The first two terms are calculated by applying the same parameters (k-point sampling, energy cutoff, etc.). The third term is the total energy of an isolated adsorbate molecule, which is estimated by putting an adsorbate molecule in a box with dimensions of 20 Å × 20.5 Å × 21 Å and carrying out a spin-polarized Γ-point calculation. With this definition, a more negative value of ΔE_{ads} corresponds to stronger binding between adsorbate and surface.

The CO_2 adsorption on the Ni(1 1 1) surface has been investigated at the threefold Fcc and Hcp, Bridge and Atop sites. After geometry optimization, CO_2 is found to be repelled towards

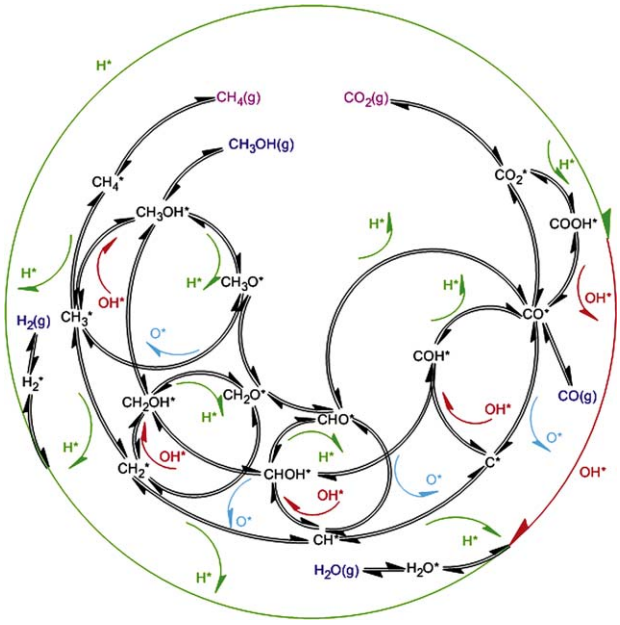

Fig. 1. Proposed mechanism for dry reforming of methane on Ni catalyst.

Table 1
Calculated adsorption energies (ΔE_{ads}) of the species involved in dry reforming of methane on Ni(1 1 1).

	Species	ΔE_{ads}[a]	Favored adsorption site
1	CH_4	−0.02	N/A
2	CH_3	−1.91	Fcc
3	CH_2	−4.01	Fcc
4	CH	−6.43	Fcc
5	C	−6.78	Hcp
6	H	−2.81	Fcc
7	O	−5.67	Fcc
8	OH	−3.42	Fcc
9	H_2O	−0.29	N/A
10	H_2	−0.22	N/A
11	CH_3OH	−0.30	N/A
12	CH_2OH	−1.54	Bridge
13	CHOH	−3.88	Fcc
14	COH	−4.39	Hcp
15	CH_3O	−2.63	Fcc
16	CH_2O	−0.75	Fcc
17	CHO	−2.26	Fcc
18	CO	−1.92	Hcp
19	CO_2	−0.02	N/A
20	COOH	−2.26	Fcc

[a] Zero-point energy correction, thermal energy correction and entropic effect are not included.

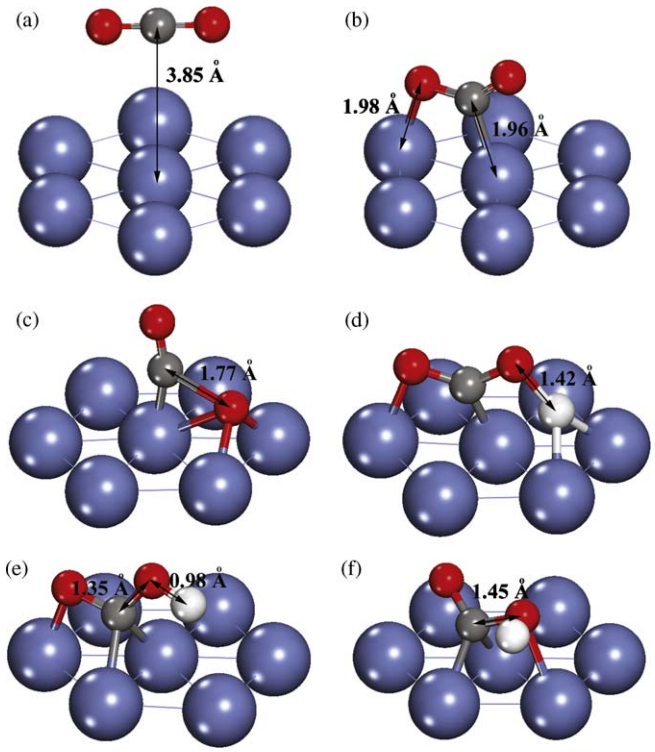

Fig. 2. Geometries of the initial states, transition states and intermediate for CO_2 decomposition on Ni(1 1 1). (a) The physisorbed CO_2 on Ni(1 1 1); (b) the chemisorbed CO_2 on Ni(1 1 1); (c) the transition state for CO_2 decomposition via the direct pathway; (d) the transition state for the H-inducted CO_2 decomposition; (e) the intermediate for the H-induced CO_2 decomposition; (f) the transition state for COOH dissociation to generate CO and OH.

vacuum if it is initially placed close to Ni(1 1 1) in a parallel manner, as shown in Fig. 2a, and the adsorption energies at all binding sites take similar small values (∼−0.02 eV), indicating the nature of the CO_2 physisorption on Ni(1 1 1). Moreover, in the presence of preliminarily adsorbed atomic H, CO_2 is further displaced apart from metal surface by 0.15 Å. However, Wang et al. [23] performed DFT calculations to reveal that covalent bonds are formed upon the CO_2 chemisorption on Ni(1 1 1). We have reproduced the most stable adsorption configuration proposed by them, as illustrated in Fig. 2b, and found this state cannot be achieved unless the CO_2 molecule is bent artificially. Wang et al. declared that their calculated adsorption energies are positive and the CO_2 chemisorption on Ni(1 1 1) is thermodynamically unfavorable. In addition, Heiland [41] has adopted the fast ion beam and fast molecular beam techniques to investigate the CO_2 dissociation, and did not detect any chemisorbed CO_2 on Ni(1 1 1) at low temperatures. Therefore, the CO_2 physisorption on Ni(1 1 1) is verified and turns out to be the precursor state to initiate the CO_2 decomposition.

By comparing the activation energy and free energy barriers at 973.15 K shown in Fig. 3, it is found that CO_2 dissociates via the direct pathway dominantly owing to the relatively high reaction rate. The corresponding configuration of the saddle point is shown in Fig. 2c, in which the cleaving C–O bond is stretched from 1.18 Å in gas phase to 1.77 Å. To facilitate the comparison, the configurations of the two saddle points and one intermediate for the H-induced CO_2 decomposition are represented in Fig. 2d–f. In these figures, one can see that CO_2 firstly approaches to the atomic H which is preliminarily adsorbed on the surface to form the COOH species, followed by the dissociation of COOH to generate CO and OH. The adsorption energies of O and OH on Ni(1 1 1) are found to be −5.67 eV and −3.42 eV (see Table 1),

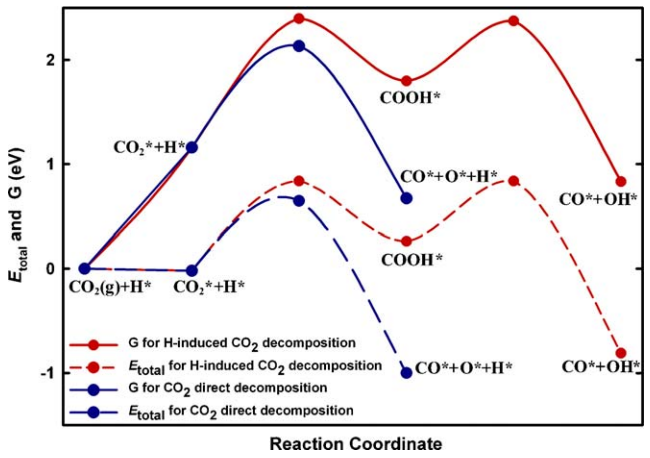

Fig. 3. Total energy and Gibbs free energy diagrams for the CO_2 direct composition and H-induced CO_2 decomposition on Ni(1 1 1).

respectively, indicating a larger site coverage of atomic O. Based on the calculated free energy barriers and adsorption energies, the primary oxidant involved in dry reforming of methane on Ni catalyst is predicted to be atomic O which is generated by the CO_2 direct decomposition. This finding agrees well with the previous kinetic and isotopic results that the CO_2 activation to produce CO and O is reversible and quasi-equilibrated under the similar reaction conditions [6]. However, we note the contribution of OH is not negligible because of the comparable barriers. Furthermore, Pan et al. [42] performed periodic DFT calculations to find on the partially hydroxylated surface of γ-Al_2O_3 which acts as the catalyst support in dry reforming of methane, the CO_2 adsorption is promoted in the vicinity of OH and simultaneously CO_2 reacts with its adjacent OH to produce a bicarbonate species.

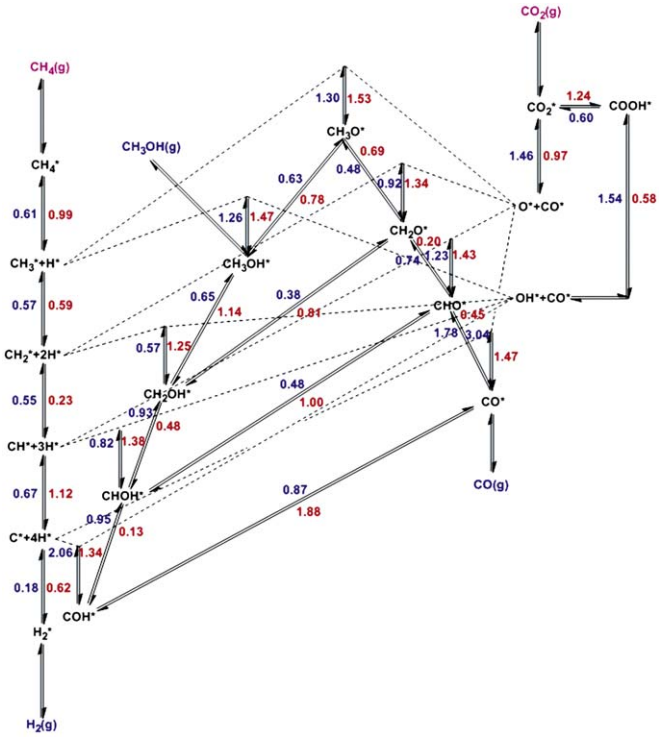

Fig. 4. Free energy barriers at 973.15 K for the forward and reverse reactions involved in dry reforming of methane.

3.2. CH_4 dissociation

Wei and Iglesia found the turnover rate of dry reforming of methane is limited solely by the C–H bond activation and unaffected by the identity as well as concentration of the co-reactants [6]. Therefore, the methane consumption is expected to take place via dissociative adsorption regardless of the existence of CO_2, and the generated CH_x intermediates are subsequently oxidized by atomic O and OH to form CH_xO and CH_xOH species, respectively. The calculated free energy barriers for all the forward and reverse reactions involved in dry reforming of methane are summarized in Fig. 4, and the corresponding activation energies are listed in Table 2.

The activation energy for the first step of CH_4 dehydrogenation is calculated to be 0.91 eV and with the zero-point energy correction considered, the barrier is lowered to 0.79 eV. This is in excellent agreement with the barrier of 0.77 ± 0.1 eV obtained in the recent experiments by Egeberg et al. [43]. Great care has been taken in their measurements to block defects on the surface with unreactive Au atoms in order to exclude the contribution of the step edge. The configuration of the transition state is shown in Fig. 5a, in which the cleaving C–H bond is stretched from 1.09 Å in gas phase to 1.61 Å. The detached H atom is located at a threefold site, and the remaining CH_3 fragment sits on the top of the adjacent surface Ni atom to achieve the maximum C–H–Ni three-center bonding [18,44]. After CH_4 is dissociatively adsorbed on the Ni surface, the further dehydrogenation of CH_3 and CH_2 species is quite easy and the generation of $CH_3O(H)$ as well as $CH_2O(H)$ is predicted to be unlikely because the free energy barriers for the CH_3 and CH_2 dissociation are 0.59 eV and 0.23 eV, much lower than those for the oxidation (1.47 eV and 1.53 eV for the CH_3 oxidation, 1.25 eV and 1.34 eV for the CH_2 oxidation). In contrast to the CH_4 dehydrogenation, the detached H atoms move to the top of surface Ni atoms, while the remaining CH_x fragments are adsorbed at the threefold sites with the cleaving C–H bonds stretched to 1.61 Å and 1.71 Å at the saddle points, as shown in Fig. 5b and c. Furthermore, the CH_2 dissociation is found to be exothermic with the reaction heat of −0.34 eV, and therefore this process is favorable both kinetically and thermodynamically.

Table 2
Calculated activation energies for all the forward ($E_{a,f}$) and reverse ($E_{a,r}$) elementary reactions involved in dry reforming of methane.

	Elementary reaction	$E_{a,f}$[a] (eV)	$E_{a,r}$[b] (eV)
1	$CH_4(g) + * \rightleftharpoons CH_4*$	0	0.02
2	$CH_4* \rightleftharpoons CH_3* + H*$	0.91	0.90
3	$CH_3* \rightleftharpoons CH_2* + H*$	0.70	0.63
4	$CH_2* \rightleftharpoons CH* + H*$	0.35	0.69
5	$CH* \rightleftharpoons C* + H*$	1.33	0.81
6	$CO_2(g) + * \rightleftharpoons CO_2*$	0	0.02
7	$CO_2* \rightleftharpoons CO* + O*$	0.67	1.65
8	$CO_2* + H* \rightleftharpoons COOH*$	1.13	0.85
9	$COOH* \rightleftharpoons CO* + OH*$	0.57	1.65
10	$CH_3* + OH* \rightleftharpoons CH_3OH*$	2.20	1.61
11	$CH_3OH* \rightleftharpoons CH_2OH* + H*$	0.88	0.69
12	$CH_2* + OH* \rightleftharpoons CH_2OH*$	1.32	0.60
13	$CH_2OH* \rightleftharpoons CHOH* + H*$	0.53	0.90
14	$CH* + OH* \rightleftharpoons CHOH*$	1.48	0.80
15	$CHOH* \rightleftharpoons COH* + H*$	0.15	0.86
16	$C* + OH* \rightleftharpoons COH*$	1.46	2.01
17	$COH* \rightleftharpoons CO* + H*$	0.98	1.97
18	$CH_3* + O* \rightleftharpoons CH_3O*$	1.59	1.31
19	$CH_3O* \rightleftharpoons CH_2O* + H*$	0.93	0.64
20	$CH_2* + O* \rightleftharpoons CH_2O*$	1.45	0.95
21	$CH_2O* \rightleftharpoons CHO* + H*$	0.36	0.74
22	$CH* + O* \rightleftharpoons CHO*$	1.53	1.08
23	$CHO* \rightleftharpoons CO* + H*$	0.20	1.48
24	$C* + O* \rightleftharpoons CO*$	1.59	2.94
25	$CH_3OH* \rightleftharpoons CH_3O* + H*$	0.89	1.38
26	$CH_2OH* \rightleftharpoons CH_2O* + H*$	0.63	1.04
27	$CHOH* \rightleftharpoons CHO* + H*$	0.71	1.14
28	$O* + H* \rightleftharpoons OH*$	1.35	1.16
29	$OH* + H* \rightleftharpoons H_2O*$	1.33	0.92
30	$H_2O* \rightleftharpoons H_2O(g)$	0.29	0
31	$H* + H* \rightleftharpoons H_2*$	0.92	0.06
32	$H_2* \rightleftharpoons H_2(g)$	0.22	0
33	$CO* \rightleftharpoons CO(g)$	1.92	0
34	$CH_3OH* \rightleftharpoons CH_3OH(g)$	0.30	0

[a,b]Zero-point energy correction, thermal energy correction and entropic effect are not included.

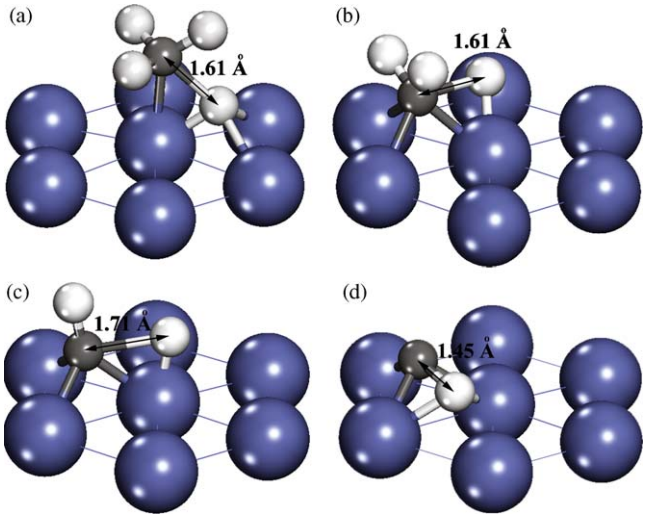

Fig. 5. Geometries of the transition states for CH_4 dissociation on Ni(1 1 1). (a) The transition state for CH_4 dehydrogenation; (b) the transition state for CH_3 dehydrogenation; (c) the transition state for CH_2 dehydrogenation; (d) the transition state for CH dehydrogenation.

As for the CH decomposition, the free energy barrier is substantially increased to 1.12 eV and remains lower than those for the CH oxidation by OH and O (1.38 eV and 1.43 eV). However, the preparation of both atomic C and CHO(H) is predicted to be likely because the two energy barriers are comparable and more importantly, the free energy barrier for the reverse reaction of the CH dehydrogenation (0.67 eV) is much lower than that for the forward reaction. Consequently, the generated C atom recombines with atomic H to form the CH species and the CH oxidation is promoted to a certain extent. As shown in Fig. 5d, the atomic C and H are adsorbed at the threefold and Bridge sites, respectively, and the cleaving C–H bond is stretched to 1.45 Å in the transition state. In fact, it is found that two saddle points are available on the potential energy surface with respect to the CH dehydrogenation step. In the other one, the atomic H moves to the top of a surface Ni atom and the C–H bond is further elongated to 1.78 Å. However, this transition state is 0.09 eV higher in total energy and is neglected in our subsequent calculation.

3.3. Oxidation of CH and C

As shown in Section 3.2, the CH species is predicted to dissociate to generate atomic C and to react with O (or OH) simultaneously. Therefore, both CH group and atomic C are taken as the candidates to be oxidized to eventually produce CO. The transition states for the reactions of C(H) with O are shown in Fig. 6a and b, in which the atomic C and O are adsorbed at the threefold hollow and adjacent Bridge sites, respectively. The distances between the atomic C and O take almost the same values (1.84 Å and 1.85 Å) in the two cases, leading to the similar free energy barriers of 1.43 eV and 1.47 eV. The corresponding final states are shown in Fig. 7a and b, and the C–O bonds are contracted to 1.29 Å and 1.20 Å to form the CHO and CO species, respectively.

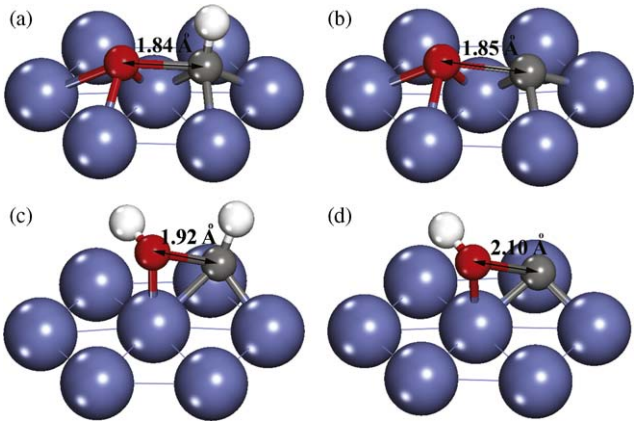

Fig. 6. Geometries of the transition states for CH and C oxidation on Ni(1 1 1). (a) The transition state for CH oxidation by O; (b) the transition state for C oxidation by O; (c) the transition state for CH oxidation by OH; (d) the transition state for C oxidation by O.

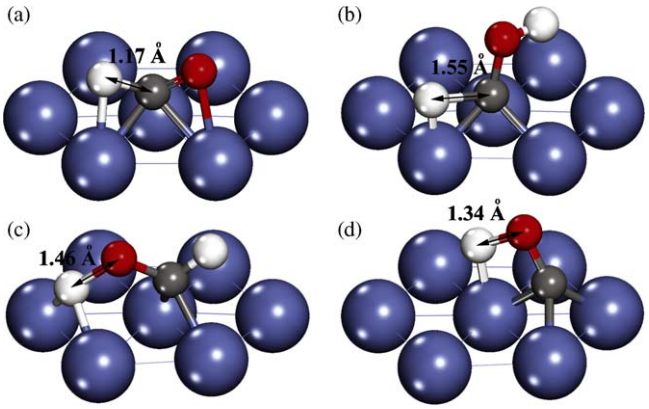

Fig. 8. Geometries of the transition states for CHO(H) and COH decomposition on Ni(1 1 1). (a) The transition state for CHO decomposition; (b) the transition state for CHOH decomposition to produce COH and H; (c) the transition state for CHOH decomposition to produce CHO and H; (d) the transition state for COH decomposition.

For the most energetically favorable structure, the CHO species is adsorbed at the Fcc site and the atomic C is coordinated with two surface Ni atoms besides the atomic O and H to keep the sp^3 hybridization. From the thermodynamic point of view, we find that the CH oxidation by O is endothermic with the reaction heat of 0.45 eV. This disagrees with what was found by Wang et al. who suggested the reaction of CH with O is favorable both kinetically and thermodynamically [24]. The discrepancy arises from the energy reference they used, which does not refer to the sum of the total energies of separated CH and O.

Then, the free energy barriers for the CH and C oxidation by OH have been calculated and found to be 1.38 eV and 1.34 eV, respectively, which are slightly lower than those for the oxidative reactions by O. However, the former pathway is not predicted to be dominant because of the low surface coverage of OH, as proposed by the previous microkinetic modeling [22]. The transition states for the CH and C oxidation by OH are shown in Fig. 6c and d, in which the OH groups move to the Atop sites adjacent to the atomic C, resulting in longer C–O bonds (1.92 Å and 2.10 Å in length) than those in the transition states for the oxidative reactions by O. In the final states, the CHOH and COH species are adsorbed at the Fcc and Hcp sites with the C–O bonds contracted to 1.37 Å and 1.34 Å, respectively, as shown in Fig. 7c and d. From the thermodynamic point of view, the reaction of CH with OH is endothermic, while the C oxidation by OH is exothermic. Thus, it is much more difficult for the COH species to dissociate to form OH along the reverse reaction of the C oxidation. As a result, the COH decomposition to produce CO is promoted to a certain extent.

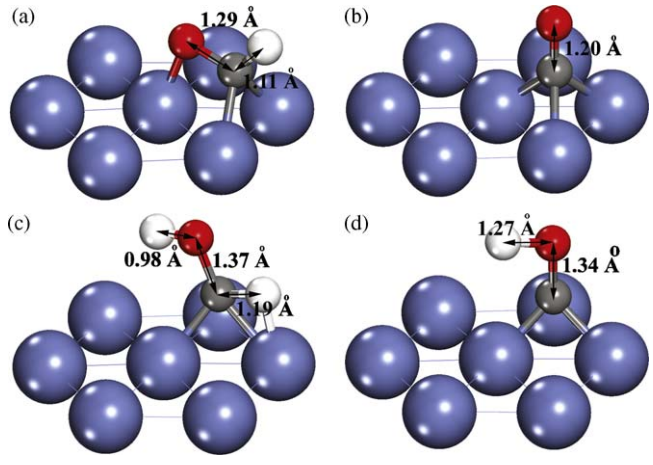

Fig. 7. Geometries of the final sates for CH and C oxidation on Ni(1 1 1). (a) CHO; (b) CO; (c) CHOH; (d) COH.

3.4. Decomposition of CHO(H) and COH

Starting from the most energetically favorable adsorption configuration, the free energy barrier and activation energy for the CHO dissociation to generate CO are calculated to be 0.45 eV and 0.20 eV, respectively, the latter being consistent with the result of 0.29 eV obtained by Wang et al. [24]. Furthermore, this reaction is found to be exothermic and release heat of 1.28 eV. Thus, the low energy barrier and high reaction heat indicate that the CHO decomposition plays a key role in producing CO and on the other hand, this kinetically and thermodynamically favored reaction would also help to remove the thermodynamic constrain in the reaction of CH with O by continuous CHO consumption. The corresponding transition state is shown in Fig. 8a, in which the activated complex is adsorbed at the Fcc site and the cleaving C–H bond is slightly stretched from 1.11 Å in the CHO adsorption configuration to 1.17 Å.

Similarly, the free energy barriers for the CHOH dissociation to form COH and CHO are found to be quite low (0.13 eV and 0.48 eV, respectively), achieving a low surface coverage of CHOH. In the transition state for the COH production, the COH species is adsorbed at the Fcc site and the detached H atom is located at the adjacent Atop site with the C–H bond stretched to 1.55 Å, as shown in Fig. 8b. Consequently, the angle of the C–O bond with respect to the surface normal is reduced to 12.27° as the repulsive interaction between COH and H is weakened. At the saddle point for the CHO production, the detached H atom is adsorbed at the Bridge site and the geometry of the CHO fragment is similar to that in the stable CHO adsorption configuration except that the atomic O is coordinated to the detached H atom with the O–H bond stretched from 0.98 Å to 1.46 Å, as shown in Fig. 8c. Furthermore, both the COH and CHO production are found to be exothermic and the reaction heats are calculated to be −0.71 eV and −0.43 eV, respectively. Therefore, these two species are readily to be generated for the subsequent dissociation once the CH group is oxidized by OH.

Finally, the free energy barrier for the COH decomposition to form CO is calculated to be 0.87 eV. In the transition state, the C–O bond is tilted to form an angle of 29.70° with respect to the surface normal in order to coordinate H with the Ni surface, and at the same time, the distance between the atomic O and H is elongated

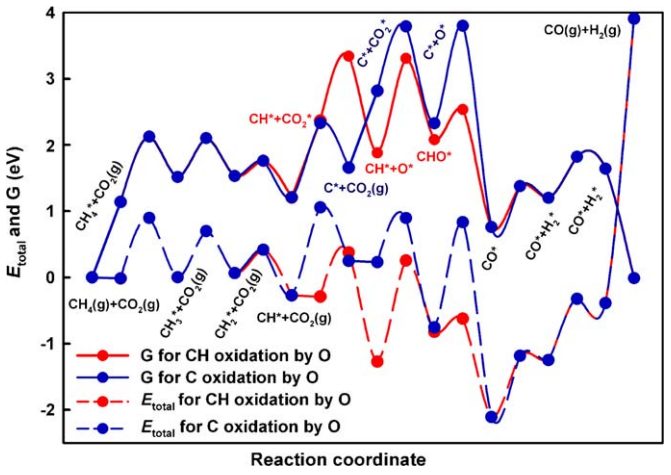

Fig. 9. Total energy and Gibbs free energy diagram at 973.15 K for dominant reaction pathways.

to be 1.34 Å, as shown in Fig. 8d. From the thermodynamic point of view, this reaction is energetically favorable and the reaction heat is calculated to be −0.99 eV, indicating both the CH and C oxidation by OH are likely to contribute to the CO production.

3.5. Dominant reaction pathway and rate-limiting step

Now that the free energy barriers for the elementary steps are evaluated by the combined DFT calculations and thermodynamic analyses, the dominant reaction pathway for dry reforming of methane is predicted to involve the direct decomposition of CO_2 to form atomic O and the dissociation of methane to generate CH and C, followed by the CH and C oxidation by atomic O, and eventually the CHO decomposition to produce CO. However, the contribution of OH cannot be negligible because the free energy barrier for the H-induced CO_2 decomposition to produce OH is comparable with that for the direct CO_2 decomposition, and the CHOH and COH dissociation are found to be favorable both kinetically and thermodynamically. This prediction agrees well with the experimental data provided by Wei and Iglesia as well as their suggested model [6].

Based on the established dominant reaction pathways, we calculate the Gibbs free energies and total energies of all relevant states (including transition states) along the reaction coordinate, as shown in Fig. 9. In such a free energy diagram, the point with the highest energy defines the slowest reaction step (at standard pressures) [45]. As one can see, the oxidation step is predicted to be the rate-limiting step for both the CH and C oxidation pathways under the current investigated conditions. However, at lower temperatures, the reaction pathway including the CH oxidation is found to be dominant because of its much lower total energy barrier than that for the C oxidation pathway, and simultaneously the CH_4 dissociation turns out to determine the overall reaction rate. This shift in rate-limiting step can be used to explain a large part of the discrepancies among the various experimental studies which are summarized in Section 1.

4. Conclusion

DFT calculations have been carried out to investigate the mechanism of dry reforming of methane. The most energetically favorable adsorption configurations have been identified for all the related substances listed in Table 1. Based on the interaction with the metal surface, these species are classified into three categories, namely the gas phase, weakly bound and tightly bound species. Then, the Gibbs free energies at 973.15 K are calculated by including the zero-point energy correction, thermal energy correction and entropic effect. The transition states for the involved elementary reactions have been explored through the dimer method and the dominant reaction pathway is constructed on the basis of the free energy barriers.

The free energy barriers for the direct CO_2 decomposition and H-induced CO_2 decomposition are calculated to be 2.13 eV and 2.40 eV, respectively. Therefore, CO_2 is predicted to dissociate via a direct pathway to generate CO and O dominantly, and atomic O is taken as the primary oxidant of CH_x intermediates. However, the H-induced CO_2 decomposition contributes to dry methane reforming as well because of the comparable barriers, and the effect of the oxidant OH is not negligible. Taking atomic O as the oxidant, we construct two dominant reaction pathways as both the CH and C oxidation are found to be likely. The reaction network begins with the CO_2 decomposition to generate O and the CH_4 dehydrogenation to produce CH and C which are subsequently oxidized by atomic O to form CHO and CO, and ends with the decomposition of CHO to produce CO and H_2. As for these two dominant reaction pathways, the oxidation step is predicted to determine the overall reaction rate under the current investigated conditions, while the CH_4 dehydrogenation is found to be the rate-limiting step at lower temperatures.

Acknowledgements

This work is supported by Doctoral Fund of Ministry of Education of China (No. 200802511007), Natural Science Foundation of Shanghai (No. 08ZR1406300) and sponsored by Shanghai Educational Development Foundation through Chenguang plan (No. 2007CG41). The computational time provided by Notur project (www.notur.no) is highly acknowledged (nn2920k and nn4685k).

References

[1] D.L. Trimm, Catal. Rev. 16 (1977) 155.
[2] J.H. McCrary, G.E. McCrary, T.A. Chubb, J.J. Nemecek, D.E. Simmons, Sol. Energy 29 (1982) 141.
[3] M. Maestri, D.G. Vlachos, A. Beretta, G. Groppi, E. Tronconi, J. Catal. 259 (2008) 211.
[4] J.F. Munera, S. Irusta, L.M. Cornaglia, E.A. Lombardo, D.V. Cesar, M. Schmal, J. Catal. 245 (2007) 25.
[5] X.E. Verykios, Appl. Catal. A: Gen. 255 (2003) 101.
[6] J. Wei, E. Iglesia, J. Catal. 224 (2004) 370.
[7] J. Wei, E. Iglesia, J. Phys. Chem. B 108 (2004) 7253.
[8] U. Olsbye, T. Wurzel, L. Mleczko, Ind. Eng. Chem. Res. 36 (1997) 5180.
[9] D.L. Trimm, Catal. Today 49 (1999) 3.
[10] S. Helveg, C. Lopez-Cartes, J. Sehested, P.L. Hansen, B.S. Clausen, J.R. Rostrup-Nielsen, F. Abild-Pedersen, J.K. Norskov, Nature 427 (2004) 426.
[11] J.R. Rostrup-Nielsen, J.H.B. Hansen, J. Catal. 144 (1993) 38.
[12] M.C.J. Bradford, M.A. Vannice, Appl. Catal. A: Gen. 142 (1996) 97.
[13] Y. Nagayasu, K. Asai, A. Nakayama, S. Iwamoto, E. Yagasaki, M. Inoue, J. Jpn. Pet. Inst. 49 (2006) 186.
[14] Y. Cui, H. Zhang, H. Xu, W. Li, Appl. Catal. A: Gen. 318 (2007) 79.
[15] G.S. Gallego, C. Batiot-Dupeyrat, J. Barrault, F. Mondragon, Ind. Eng. Chem. Res. 47 (2008) 9272.
[16] J. Juan-Juan, M.C. Roman-Martinez, M.J. Illan-Gomez, Appl. Catal. A: Gen. 355 (2009) 27.
[17] R.M. Watwe, H.S. Bengaard, J.R. Rostrup-Nielsen, J.A. Dumesic, J.K. Norskov, J. Catal. 189 (2000) 16.
[18] A. Michaelides, P. Hu, Surf. Sci. 437 (1999) 362.
[19] A. Michaelides, P. Hu, J. Chem. Phys. 112 (2000) 8120.
[20] A. Michaelides, P. Hu, J. Chem. Phys. 112 (2000) 6006.
[21] H.S. Bengaard, J.K. Norskov, J. Sehested, B.S. Clausen, L.P. Nielsen, A.M. Molenbroek, J.R. Rostrup-Nielsen, J. Catal. 209 (2002) 365.
[22] D.W. Blaylock, T. Ogura, W.H. Green, G.J.O. Beran, J. Phys. Chem. C 113 (2009) 4898.
[23] S. Wang, D. Cao, Y. Li, J. Wang, H. Jiao, J. Phys. Chem. B 109 (2005) 18956.
[24] S. Wang, X. Liao, J. Hu, D. Cao, Y. Li, J. Wang, H. Jiao, Surf. Sci. 601 (2007) 1271.
[25] G. Henkelman, H. Jonsson, J. Chem. Phys. 111 (1999) 7010.
[26] X.E. Verykios, Int. J. Hydrogen Energy 28 (2003) 1045.
[27] G. Kresse, J. Hafner, Phys. Rev. B 47 (1993) 558.
[28] G. Kresse, J. Hafner, Phys. Rev. B 49 (1994) 14251.
[29] G. Kresse, J. Furthmüller, Comp. Mater. Sci. 6 (1996) 15.
[30] G. Kresse, J. Furthmüller, Phys. Rev. B 54 (1996) 11169.
[31] P.E. Blöchl, Phys. Rev. B 50 (1994) 17953.
[32] G. Kresse, D. Joubert, Phys. Rev. B 59 (1999) 1758.

[33] J.P. Perdew, K. Burke, M. Ernzerhof, Phys. Rev. Lett. 77 (1996) 3865.
[34] D. Sheppard, R. Terrell, G. Henkelman, J. Chem. Phys. 128 (2008) 10.
[35] H.J. Monkhorst, J.D. Pack, Phys. Rev. B 13 (1976) 5188.
[36] M. Methfessel, A.T. Paxton, Phys. Rev. B 40 (1989) 3616.
[37] G. Kresse, J. Hafner, Surf. Sci. 459 (2000) 287.
[38] S. Stolbov, S. Hong, A. Kara, T.S. Rahman, Phys. Rev. B 72 (2005) 155423.
[39] Y. Zhu, X. Zhou, D. Chen, W. Yuan, J. Phys. Chem. C 111 (2007) 3447.
[40] D.L. Lide, CRC Handbook of Physics and Chemistry, Academic Press, 1997.
[41] W. Heiland, Surf. Sci. 251–252 (1991) 942.
[42] Y. Pan, C. Liu, Q. Ge, Langmuir 24 (2008) 12410.
[43] R.C. Egeberg, S. Ullmann, I. Alstrup, C.B. Mullins, I. Chorkendoff, Surf. Sci. 497 (2002) 183.
[44] Y. Zhu, Y. Dai, D. Chen, W. Yuan, J. Mol. Catal. A: Chem. 264 (2007) 299.
[45] M.P. Andersson, E. Abild-Pedersen, I.N. Remediakis, T. Bligaard, G. Jones, J. Engbwk, O. Lytken, S. Horch, J.H. Nielsen, J. Sehested, J.R. Rostrup-Nielsen, J.K. Norskov, I. Chorkendorff, J. Catal. 255 (2008) 6.